Efficient removal of chromium from water by Mn₃O₄@ZnO/Mn₃O₄ composite under simulated sunlight irradiation: Synergy of photocatalytic reduction and adsorption

Ning Li[a], Yu Tian[a,*], Jianhui Zhao[a], Jian Zhang[a], Jun Zhang[a], Wei Zuo[a], Yi Ding[b]

[a] State Key Laboratory of Urban Water Resource and Environment (SKLUWRE), School of Environment, Harbin Institute of Technology, Harbin, 150090, China
[b] Marine College, Shandong University at Weihai, Weihai, 264209, China

ARTICLE INFO

ABSTRACT

A novel Mn₃O₄@ZnO/Mn₃O₄ composite was designed to remove Cr (VI) and Cr (III) from water by concurrent photocatalysis and adsorption. The Mn₃O₄@ZnO photocatalyst with core-shell nano-sphere structure, was first fabricated by precisely controlled process using a mild hydrothermal method combined with atomic layer deposition (ALD). The wurtzite ZnO layer was uniformly deposited on haus-mannite Mn₃O₄ surface, which formed a typical II-type heterojunction, separating the photo-generated electron-hole pairs effectively. Hence, rapid Cr (VI) reduction by Mn₃O₄@ZnO under simulated sunlight irradiation was achieved at 95.3% in 110 min. The pure Mn₃O₄ as adsorbent could subsequently adsorb the reduced Cr (III) from aqueous solution. Noticeably, the total Cr removal efficiency was enhanced to 92.0% within 70 min by concurrent photocatalysis and adsorption compared to 88.8% even within 120 min in the separate two processes. Mechanism exploration proposed that more active sites on Mn₃O₄@ZnO surface would be released for continuous photocatalytic reduction of Cr (VI) after the transfer of reduced Cr (III) from Mn₃O₄@ZnO onto Mn₃O₄ surface. In addition, the synergy of photocatalysis and adsorption on Cr removal was the strongest at pH = 6.0 and the highest removal efficiency of 96.0% was realized within 70 min. The outstanding synergistic effect of photocatalytic reduction and adsorption makes the innovative Mn₃O₄@ZnO/Mn₃O₄ composite a promising candidate for Cr remediation in aquatic environment.

© 2017 Elsevier B.V. All rights reserved.

1. Introduction

Hexavalent chromium (Cr (VI)) has been widely utilized in numerous industrial processes including metal processing, electroplating and mining [1–3]. Large amounts of Cr-containing wastewater discharges from these industries without reasonable treatment, which poses serious threats to the environment as well as to the human beings due to its strong toxicity, carcinogenicity, mobility and undegradability [4,5]. The two primary forms of Cr (VI) and trivalent chromium (Cr (III)) usually exist in water solution. As is well known, Cr (VI) is more toxic and mobile than Cr (III) [6]. Consequently, Cr (VI) reduction seems to be an effective strategy for toxicity reduction, which has received considerable attention [7,8]. Various approaches including chemical reduction and precipitation have been developed for Cr (VI) removal from

aqueous environment [9,10]. However, these traditional methods generally have some shortcomings such as incomplete removal, low efficiency and high energy consumption, posing a key obstacle to the extensive applications [11]. Notably, photocatalytic reduction and adsorption are regarded as green technologies for efficient elimination of Cr contaminants.

Photocatalytic reduction draws increasing attentions with great advantages of free secondary pollution and mild reaction conditions [12,13]. When the photocatalyst is irradiated by photons with energy higher than the band gap, electrons could be generated in the conduction band and served as reducing species for Cr (VI) elimination in aquatic environment [14]. Unfortunately, traditional single-component photocatalysts such as TiO₂, WO₃ and Fe₂O₃ usually exhibit less catalytic active sites and narrow light response in the ultraviolet region, thereby limiting the photocatalytic activity and widespread applications in sunlight [15–17]. Moreover, the combination of photo-induced carriers was more likely occurred in the single-component photocatalyst [18]. The opportunities to react between electrons and Cr (VI) anions were reduced, decreasing the photocatalytic

activity. Several noble metal loaded photocatalysts have been developed to improve photocatalytic performance. For instance, the Ag@Fe$_3$O$_4$@SiO$_2$@TiO$_2$ and TiO$_2$/Ag photocatalysts with superior reduction property were fabricated [19,20]. However, the high cost limits their widely practical applications. Moreover, intensive efforts have been invested in photocatalytic reduction of Cr (VI) without further removal of reduced Cr (III) [21,22]. Although the toxicity of Cr (III) declines compared to that of Cr (VI), the presence of Cr (III) displays great potential risks as Cr (III) may be reoxidized to Cr (VI) during further water treatment process such as chlorination [23]. Additionally, adsorption also plays an important role in heavy metal removal from industrial wastewater [24]. Adsorbents with large specific surface area and strong combining ability could realize high adsorption performance. Nevertheless, conventional adsorbents mostly concentrate on porous materials such as activated carbon, zeolites and silicon dioxide [25]. The adsorption rate was limited due to the dominant active sites within the pores. Thus, designing a high-performance system for concurrent Cr (VI) and Cr (III) removal by photocatalysis and adsorption has been an intensively pursued topic.

Manganous-manganic oxide (Mn$_3$O$_4$), as a p-type semiconductor, has been synthesized as co-catalyst to extend light-harvesting range, and thus enhance photocatalytic activity [26]. As reported in the previous literature, Mn$_3$O$_4$ photocatalyst has great potential in promoting oxygen evolution in the nanocomposites, which provides a new way to prepare efficient photocatalysts instead of noble metal doped ones [27]. Zinc oxide (ZnO), as an n-type semiconductor, offers considerable advantages such as inexpensive, high quantum efficiency and environment-friendly features, which has been widely employed for photocatalysis [28,29]. The two in combination could expand the optical response scope. What's more, the valance band and conduction band energies of ZnO are more positive than the corresponding energies of Mn$_3$O$_4$ [30]. The separation of photo-induced carriers could be promoted and the electrons would be accumulated on the conduction band of ZnO with light

irradiation. If ZnO is fully designed on the surface of Mn$_3$O$_4$, Cr (VI) reduction with potential high efficiency is of great interest. In this research, the Mn$_3$O$_4$ with large surface area was employed as adsorbent for Cr (III) removal, which was synthesized by hydrothermal method. The three-dimensional (3D) Mn$_3$O$_4$@ZnO core-shell photocatalyst was precisely designed via hydrothermal and atomic layer deposition (ALD) method. The uniform ultrathin ZnO layer deposited on Mn$_3$O$_4$ surface by ALD would facilitate charge separation. The photo-generated electrons could be quickly transferred to ZnO surface for Cr (VI) reduction. The photocatalytic reduction property of Mn$_3$O$_4$@ZnO photocatalyst, adsorption performance of Mn$_3$O$_4$ for Cr removal and the relevant mechanism were first reported in this study.

Herein, a novel Mn$_3$O$_4$@ZnO/Mn$_3$O$_4$ composite was employed for Cr removal by photocatalytic reduction and adsorption. The aim of this study was to realize efficient removal of Cr (VI) and Cr (III) from water. Highly efficient removal of Cr was achieved and accelerated by synergetic effects of Mn$_3$O$_4$@ZnO photocatalyst and Mn$_3$O$_4$ adsorbent. This study was mainly focused on: 1) characterization of the newly-designed Mn$_3$O$_4$@ZnO photocatalyst and Mn$_3$O$_4$ adsorbent; 2) Cr removal from water solution by photocatalytic reduction and adsorption; 3) Effects of pH on Cr removal by Mn$_3$O$_4$@ZnO/Mn$_3$O$_4$ composite; 4) Mechanism exploration of the enhanced Cr removal efficiency. This work demonstrated that the Mn$_3$O$_4$@ZnO/Mn$_3$O$_4$ composite was a promising candidate for efficient removal of total Cr under simulated sunlight irradiation.

2. Experimental

2.1. Materials and reagents

Manganese chloride (MnCl$_2$·4H$_2$O) and sodium hydroxide (NaOH) (Sinopharm, Shanghai) were chosen as reactants for Mn$_3$O$_4$ preparation. Poly (vinylpyrrolidone) (PVP 40, Sigma) was employed as surface active agent during the synthesis process. Diethylzinc (DEZ, Sigma) and deionized (DI) water were utilized for ZnO
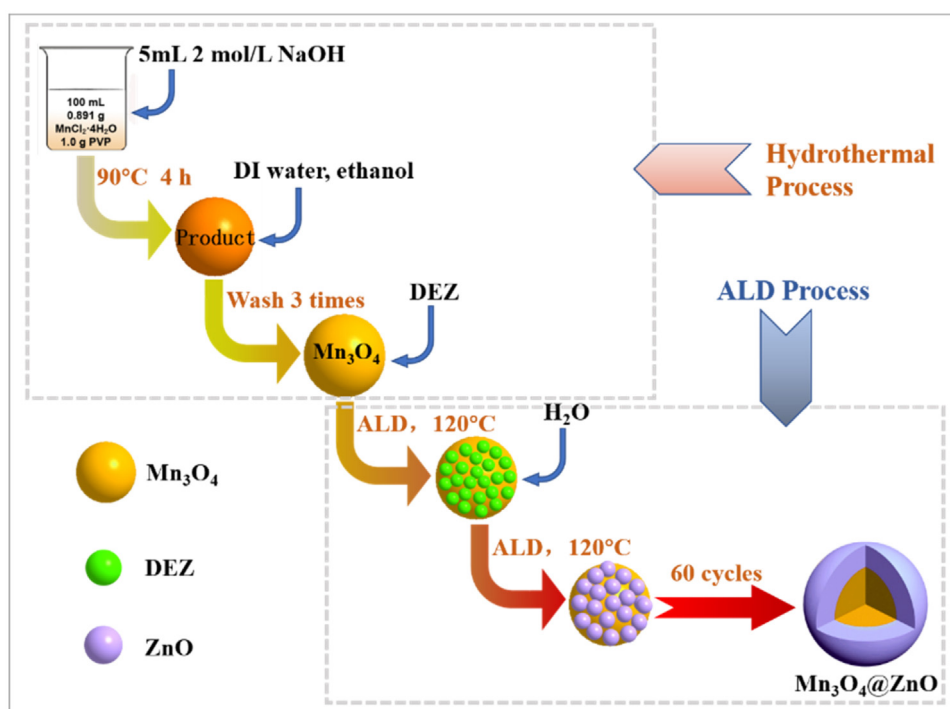

Fig. 1. Schematic diagram for fabrication of Mn$_3$O$_4$ and Mn$_3$O$_4$@ZnO.

shell deposition. Other chemicals including ethanol and potassium dichromate ($K_2Cr_2O_7$) were provided by Xilong Chemical Co., Ltd. Nitrogen (N_2, 99.9%, LiMing Gas) was supplied as careering gas and purging gas in the atomic layer deposition (ALD) process.

2.2. Synthesis

The Mn_3O_4 nanoparticles were prepared with hydrothermal method. The Mn_3O_4@ZnO photocatalyst was fabricated through depositing ZnO layer on Mn_3O_4 surface by ALD method. The DI water was applied as solvent in the whole synthetic process. The synthesis processes of Mn_3O_4 and Mn_3O_4@ZnO were shown in Fig. 1.

2.2.1. Synthesis of Mn_3O_4 adsorbent

The mixed solution (100 mL) containing 0.891 g $MnCl_2 \cdot 4H_2O$ and 1.0 g PVP was transferred to a glass bottle and heated to 90 °C in a magnetic stirring heater. Immediately, 2.0 mol/L NaOH with the volume of 5.0 mL was added to the bottle. At this moment, reactions proceed rapidly and brown precipitate appeared. Then the generated precipitate was further heated and stirred for another 4 h during maturing process. The target product was cooled down to room temperature before thrice wash using DI water and ethanol, respectively. At last, the cleaned product was dried in an electric dry oven.

2.2.2. Synthesis of Mn_3O_4@ZnO photocatalyst

The Mn_3O_4 core was fabricated with the same operation as the Mn_3O_4 adsorbent. The ZnO shell was uniformly deposited on Mn_3O_4 surface at 120 °C in an ALD reactor (MNT, Wuxi, China). DEZ and DI water were applied as zinc and oxygen precursors. A certain thickness of ZnO layer would appear on Mn_3O_4 surface after 60 cycles of deposition. The deposition rate (v) can be calculated according to the number of deposition cycles (N), diameters of Mn_3O_4 (D1) and Mn_3O_4@ZnO (D2) nanoparticles: $v = (D2-D1)/2/N$. The detailed information (ALD process and possible reaction equations) for Mn_3O_4@ZnO preparation and mole ratio of Mn_3O_4 and ZnO (3.2:1) determination in Mn_3O_4-ZnO composite were described in Supporting Information (SI). Pure ZnO was also prepared by ALD for optical property study.

2.3. Characterization

The crystal structure of the as-prepared nanoparticles were identified by X-ray diffraction (XRD) measurement using a diffractometer (Empyrean, Netherlands) with Cu Kα radiation

($\lambda = 1.5414 \text{ Å}$). The X-ray photoelectron spectroscopy (XPS) profile of all samples were recorded via an XPS spectrometer (PHI 5700, US) with Al Kα excitation. All peak energies obtained in this study were calibrated based on the energy of external carbon (284.8 eV). The specific surface area of the samples were obtained through Brunauer-Emmett-Teller (BET) method using N_2 adsorption-desorption isotherms by a Micromeritics analyzer (ASAP 2020, US) at 77 K. The surface morphology, micro-structure and crystalline phase of samples were analyzed by a Field Emission Scanning Electron Microscope (FESEM, HELIOS 600i, Netherlands) at 20 kV and a Field Emission Transmission Electron Microscope (FETEM, TecnaiF2F30, Netherlands) at 200 kV. All samples for SEM observation were pre-coated with a gold layer to enhance conductivity. Besides, the samples for TEM analyses were dispersed in ethanol and dropped on a copper grid before observation. The ultraviolet-visible (UV-vis) diffuse reflectance spectra of the nanomaterials were recorded using an UV–vis spectrophotometer (UV 2550, Japan). A zetasizer (Malvern, UK) was used for zeta potential measurement of the samples. The photocurrents and electrochemical impedance spectroscopy (EIS) were recorded using a standard three-electrode cell by an electrochemical system (CH1660E, China). The photoluminescence (PL) spectra of the samples were collected by a fluorescence spectrometer (F4600, Japan).

2.4. Photocatalytic reduction and adsorption experiments

The Cr (VI) and Cr (III) removal by photocatalysis and adsorption were performed in a photoreactor (NBeT Group Corp., China) equipped with a Xe lamp (300 W) and an optical filter (UVCUT 450). The reaction temperature was maintained at 25 °C through recycling the condensed water around the quartz reactor. The distance between light source and the sample was 10 cm. The light intensity was determined as 900 mW/cm^2. During separate processes of photocatalysis and adsorption, Mn_3O_4@ZnO photocatalyst was firstly added into the reactor with 200 mL Cr (VI) solution (10 mg/L) and stirred for 180 min in dark to reach equilibrium. After that, the sunlight was irradiated for 110 min. Then Mn_3O_4 adsorbent was added into the solution and stirred for another 50 min in dark. The dosage ratio of Mn_3O_4@ZnO and Mn_3O_4 was set at 1:1, 2:1, 3:1 (molar ratio), and the optimum dosage of Mn_3O_4 adsorbent was determined as 0.15 g/L based on pre-experiments (Fig. S1, SI). The samples were withdrawn at preset time intervals.

During the concurrent process of photocatalysis and adsorption, 200 mL Cr (VI) solution (10 mg/L), a certain amount of Mn_3O_4@ZnO and Mn_3O_4 (Mn_3O_4 concentration was 0.15 g/L, molar ratio of Mn_3O_4@ZnO and Mn_3O_4 was 2:1) were added into the reactor with stirring for 180 min in dark. Then the mixture was irradiated with sunlight for 100 min. The water samples were withdrawn at certain intervals during illumination. All of the collected samples were filtered by cellulose acetate membranes (0.45 μm) for Cr (VI) and Cr (III) measurement. In order to eliminate the effect of photolysis, Cr solution without photocatalyst or adsorbent addition was used as blank. The total concentration of Cr (C_T) was measured by inductively coupled plasma mass spectrometry (ICP-MS). The Cr (VI) concentration (C_1) was obtained using the diphenyl hydrazine method [31]. Then the Cr (III) concentration (C_2) could be calculated by the equation: $C_2 = C_T - C_1$.

The Mn_3O_4 and Mn_3O_4@ZnO mixture was centrifugalized and dried at 60 °C after concurrent photocatalysis and adsorption. The mixture was first washed using 0.1 mol/L HNO_3 for 6 h to desorb Cr (III). After that, the nanoparticles were washed with DI water to remove residual HNO_3. Then the mixture was added into 0.1 mol/L NaOH solution and washed for another 6 h to realize Mn_3O_4@ZnO regeneration. At last, the materials were also washed with DI water to remove residual NaOH. For the reusability of the
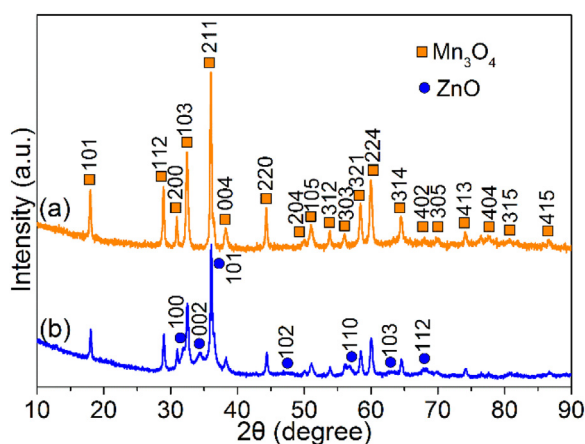
Fig. 2. XRD patterns of (a) Mn_3O_4 adsorbent and (b) Mn_3O_4@ZnO photocatalyst.

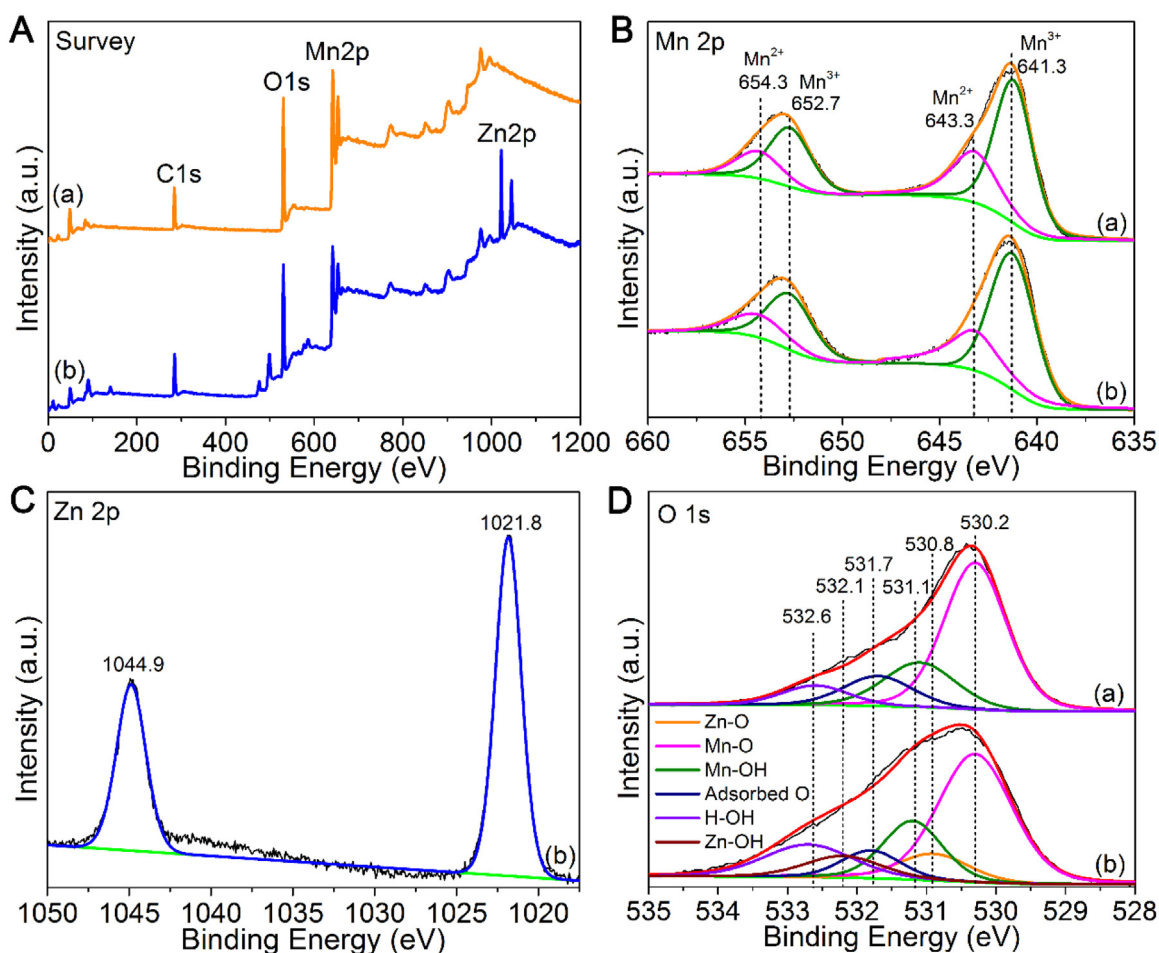**Fig. 3.** XPS spectra of (A) survey; high resolution of (B) Mn 2p, (C) Zn 2p and (D) O 1 s for (a) Mn_3O_4 adsorbent and (b) Mn_3O_4@ZnO photocatalyst.

Mn_3O_4@ZnO/Mn_3O_4 nanoparticles, the operation process was as same as that of its initial use.

3. Results and discussion

3.1. Characterization of Mn_3O_4 and Mn_3O_4@ZnO

The crystal structure of the as-synthesized nanomaterials were identified by XRD measurement, and the results were presented in Fig. 2. Evidently, the diffraction peaks displayed in Fig. 2a matched well with tetragonal hausmannite structure (JCPDS NO. 24-0734), confirming the successful synthesis of Mn_3O_4. In comparison with Fig. 2a, the crystal phase of Mn_3O_4 had no change in Fig. 2b. Only slightly weakened peak intensity was observed due to new layer deposited on Mn_3O_4 surface. Moreover, several new characteristic peaks at 31.7° (100), 34.4° (002), 36.2° (101), 47.5° (102), 56.6° (110), 62.9° (103) and 68.0° (112) appeared in Fig. 2b, corresponding to hexagonal wurtzite ZnO (JCPDS NO. 36-1451). These peak values were also in accordance with previous reports [32,33].

The chemical composition and valance state of the as-prepared nanomaterials were confirmed through XPS analysis. The XPS survey scan and high resolution spectra of Mn 2p, Zn 2p and O 1 s were shown in Fig. 3. As presented in Fig. 3A, the two samples displayed similar signals of O 1 s and Mn 2p. The significant difference was related to Zn 2p peak appearing on the composite nanoparticles fabricated by hydrothermal and atomic layer deposition (ALD) methods. The Mn 2p peak energies of the two samples

were almost identical (Fig. 3B), revealing the valence states of Mn remained the same after further designing by ALD. Besides, the high resolution Mn 2p spectra consisted of Mn 2p1/2 and Mn 2p3/2 peaks with an energy separation of 11.6 eV. The Mn 2p1/2 and Mn 2p3/2 peaks were deconvoluted into two peaks located at 654.3 and 652.7 eV, 643.3 and 641.3 eV, which were assigned to Mn^{2+} 2p1/2 and Mn^{3+} 2p1/2, Mn^{2+} 2p3/2 and Mn^{3+} 2p3/2 respectively. The similar results were also found in previous literatures [1,34]. Notably, the ratio of Mn^{2+} and Mn^{3+} was calculated to be about 1:2 according to the corresponding peak areas, indicating the successful fabrication of Mn_3O_4 [34]. As shown in Fig. 3C, two main peaks of Zn 2p1/2 and Zn 2p3/2 were centered at 1044.9 and 1021.8 eV, which were recognized as Zn^{2+} [35]. The O 1 s spectra of Mn_3O_4 sample was resolved into four peaks at binding energies of 530.2, 531.1, 531.7 and 532.6 eV (Fig. 3D), corresponding to lattice oxygen of Mn-O bonds, hydroxyl on the Mn_3O_4 surface, adsorbed oxygen and water molecules respectively [34]. Comparatively, the O 1 s spectra of Mn_3O_4@ZnO exhibited another two peaks with binding energies of 530.8 and 532.1 eV, which were belonged to lattice oxygen of Zn-O and hydroxyl on the ZnO surface, respectively [32]. The Mn-O and Zn-O bonds and hydroxyl in Mn_3O_4 and Mn_3O_4@ZnO were further identified by Fourier transformation infrared spectroscopy (FTIR) analysis (Fig. S2, SI).

The morphology of Mn_3O_4 and Mn_3O_4@ZnO were examined through FESEM and FETEM observation. It can be clearly seen from SEM images (Fig. S3A) and TEM images (Fig. 4A) that the as-

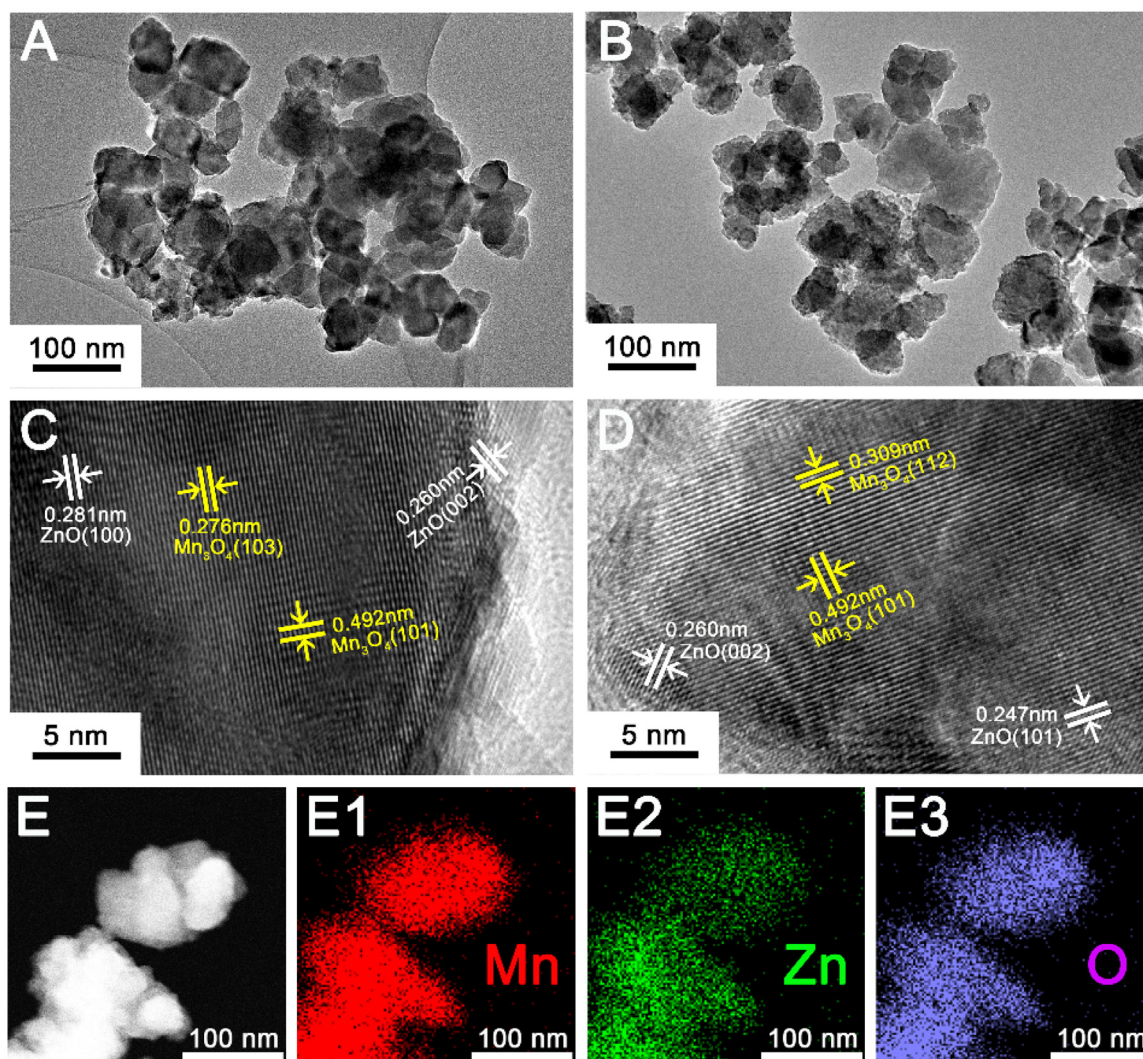**Fig. 4.** TEM images of (A) Mn_3O_4 and (B) Mn_3O_4@ZnO; HRTEM images of (C-D) Mn_3O_4@ZnO; TEM mapping of (E) Mn_3O_4@ZnO: (E1) Mn, (E2) Zn, (E3) O elements.

prepared Mn_3O_4 were nano-spheres with diameter ranging from 32 to 38 nm. The sphere-like morphology was perfectly preserved after ZnO deposition by ALD (Fig. 4B and Fig. S3B). Only the diameter of Mn_3O_4@ZnO (Mn_3O_4: ZnO=2:1) spheres slightly increased to 48–56 nm with 60 cycles of ZnO deposition. The deposition rate of ZnO was calculated to be about 0.13 nm/cycle. High-resolution TEM (HRTEM) images of Mn_3O_4@ZnO sample were recorded and presented in Fig. 4(C–D). The lattice fringes with spacing of 0.492, 0.309 and 0.276 nm corresponded to (101), (112) and (103) crystal planes of the tetragonal hausmannite Mn_3O_4 [36]. Besides, another three lattice fringes appeared at the edge of the nanosphere. The lattice spacings were measured as 0.247, 0.260 and 0.281 nm, which could be ascribed to (101), (002) and (100) planes of wurtzite ZnO [37]. These results were in agreement with the XRD analysis, which further confirmed the successful deposition of ZnO layer on the Mn_3O_4 surface. The TEM element mapping of Mn, Zn and O were also conducted to study the elements distribution in Mn_3O_4@ZnO. As shown in Fig. 4(E1–E3), the red, green and blue dots with bright color on the black background represented Mn, Zn and O elements respectively. It could be clearly seen that the three elements were uniformly distributed on the randomly selected area, indicating the uniform growth of ZnO shell layer on the Mn_3O_4 core surface [29].

The surface area of Mn_3O_4 and Mn_3O_4@ZnO were calculated by Brunauer-Emmett-Teller (BET) method [38]. The N_2 adsorption-desorption isotherms were shown in Fig. S4, which matched typical type-IV classification according to hysteresis loops listed by IUPAC [38]. The specific surface area of the Mn_3O_4 nanoparticles was determined as $54.3\,m^2/g$. It was worth noting that the Mn_3O_4@ZnO composite exhibited considerably enhanced surface area of $98.0\,m^2/g$. This phenomenon was mostly ascribed to the weakened particle aggregation after ZnO layer uniformly deposited on Mn_3O_4 surface. The larger surface area means more active sites on the Mn_3O_4@ZnO surface, which could be provided for adsorption and photocatalysis.

3.2. Cr removal by photocatalysis and adsorption

Cr removal was first studied with different molar ratios of Mn_3O_4@ZnO and Mn_3O_4 by separate processes of photocatalytic reduction and adsorption. Cr (VI) solution without Mn_3O_4@ZnO or Mn_3O_4 addition was used as a blank. Variation of total Cr, Cr (VI) and Cr (III) concentrations as a function of time were shown in Fig. 5. Cr (VI) was dramatically reduced to Cr (III) via Mn_3O_4@ZnO core-shell photocatalyst under simulated sunlight irradiation. Comparably, no obvious change of Cr concentration

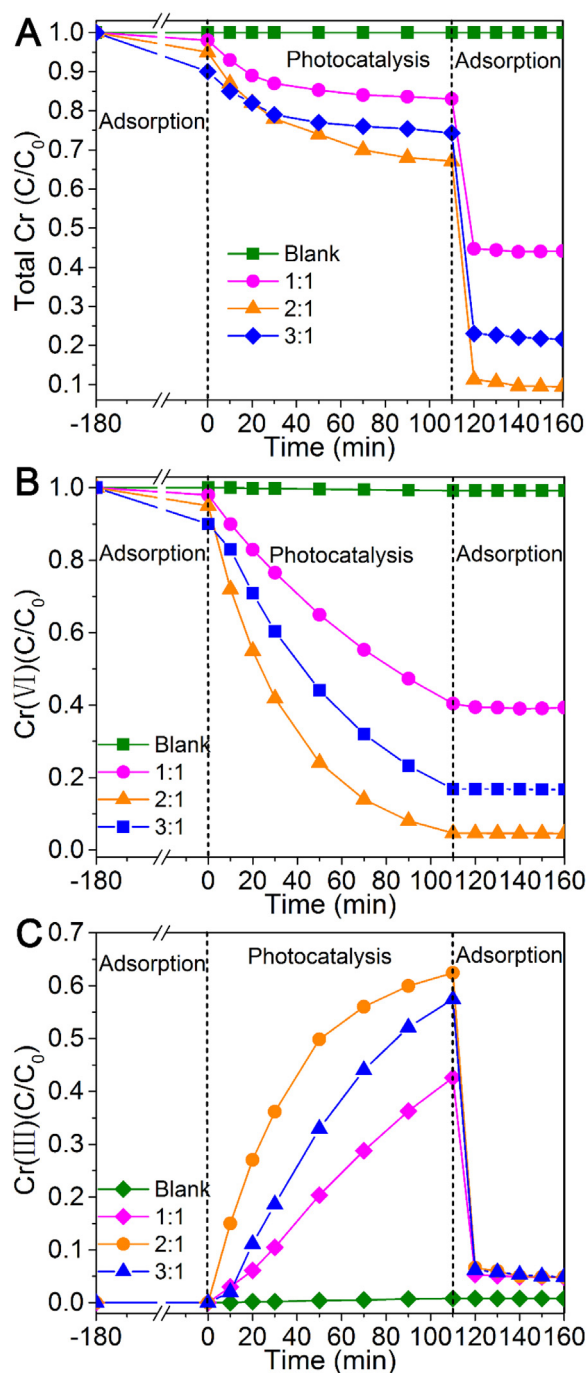**Fig. 6.** Cr removal with concurrent photocatalysis and adsorption by Mn$_3$O$_4$@ZnO/Mn$_3$O$_4$ composite. Initial conditions: [Cr (VI)] = C$_0$ = 10 mg/L, [Mn$_3$O$_4$] = 0.15 g/L, Mn$_3$O$_4$@ZnO: Mn$_3$O$_4$ = 2:1, solution pH = 6.5.

Fig. 5. Cr removal with separate processes of photocatalysis and adsorption at different molar ratios of Mn$_3$O$_4$@ZnO and Mn$_3$O$_4$ (A) Total Cr, (B) Cr (VI), (C) Cr (III). Initial conditions: [Cr (VI)] = C$_0$ = 10 mg/L, [Mn$_3$O$_4$] = 0.15 g/L, solution pH = 6.5.

was observed for the blank in the whole process. The results suggested that it was not photolysis but the photocatalysis that played a significant role in Cr reduction [39]. The Mn$_3$O$_4$@ZnO photocatalyst with dosage of 0.4 g/L (Mn$_3$O$_4$@ZnO: Mn$_3$O$_4$ = 2:1) exhibited superior photocatalytic activity. The reduction rate of Cr (VI) reached 95.3% within 110 min, which was higher than those obtained for Mn$_3$O$_4$@ZnO: Mn$_3$O$_4$ = 1:1 (59.6%) and Mn$_3$O$_4$@ZnO: Mn$_3$O$_4$ = 3:1 (83.2%). It can be inferred that less active sites for photocatalysis were provided when adding a small amount of Mn$_3$O$_4$@ZnO. Besides, catalyst agglomeration or light blocking would occur with overweight Mn$_3$O$_4$@ZnO addition, declining the

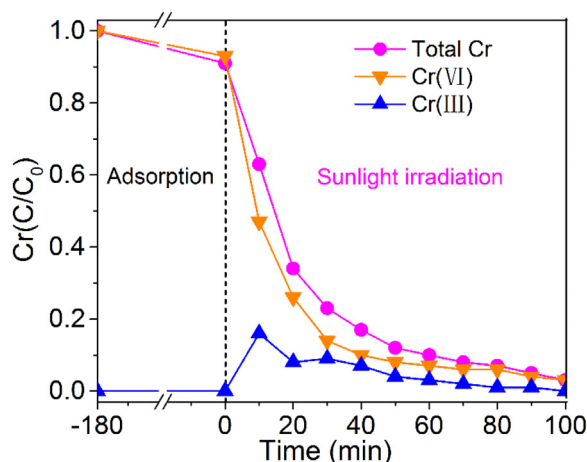photocatalytic activity. Cr (III) was accumulated gradually in the system while total Cr concentration decreased during photocatalytic reduction. The decreased concentration of total Cr might attribute to Cr (III) adsorption onto the Mn$_3$O$_4$@ZnO surface. During the subsequent adsorption with Mn$_3$O$_4$, the concentration of total Cr witnessed a sharp decline in the first 10 min and remained stable within 20 min. In comparison with the concentrations of Cr (VI) and Cr (III) in the final adsorption process, it was obvious that the total Cr removal was mainly resulted from Cr (III) adsorption. Considering the adsorption rate of Cr (III) was faster than the photocatalytic reduction rate of Cr (VI), Cr (VI) reduction became the limiting step in the whole process for Cr removal. Based on the total Cr removal rate by separate processes of photocatalysis and adsorption, the optimum mole ratio of Mn$_3$O$_4$@ZnO and Mn$_3$O$_4$ was set at 2:1. Higher removal rates of total Cr and Cr (VI) with 90.5% and 95.4% at Mn$_3$O$_4$@ZnO: Mn$_3$O$_4$ = 2:1 was realized within 160 min.

Fig. 6 presented the variation of Cr concentration in the process of concurrent photocatalysis and adsorption. Evidently, the removal efficiency of total Cr and Cr (VI) were improved considerably compared to the results obtained in the separate processes. Specially, the removal rate of total Cr was up to 92.0% with simulated sunlight irradiation for 70 min by concurrent photocatalysis and adsorption. The Cr (VI) reduction efficiency was 94.0% at this moment. However, the total Cr displayed only 88.8% removal within 120 min in the separate two processes. It was worth noting that the reduction rate of Cr (VI) was enhanced and little Cr (III) was accumulated in the system. The reason might be that the reduced Cr (III) desorbed from Mn$_3$O$_4$@ZnO surface and active sites could be available for continuous photocatalysis. The mechanism of Cr removal would be discussed in detail in part 3.4.

The cycle experiment for Cr removal was conducted after Mn$_3$O$_4$@ZnO and Mn$_3$O$_4$ regeneration to investigate their reusability. The variation of total Cr concentration was recorded for 70 min with five times' recycle of Mn$_3$O$_4$@ZnO and Mn$_3$O$_4$ under simulated sunlight irradiation. As shown in Fig. 7, the variation of total Cr concentrations in every cycle was similar. The total Cr removal rate was still up to 90.6% after recycling for five times, with a slight decrease of 1.4% compared to that for the first use. Additionally, the crystal structure and surface morphology of Mn$_3$O$_4$@ZnO/Mn$_3$O$_4$ remained almost unchanged after five cycles of concurrent photocatalysis and adsorption process (Fig. S5 and S6, SI), indicating both
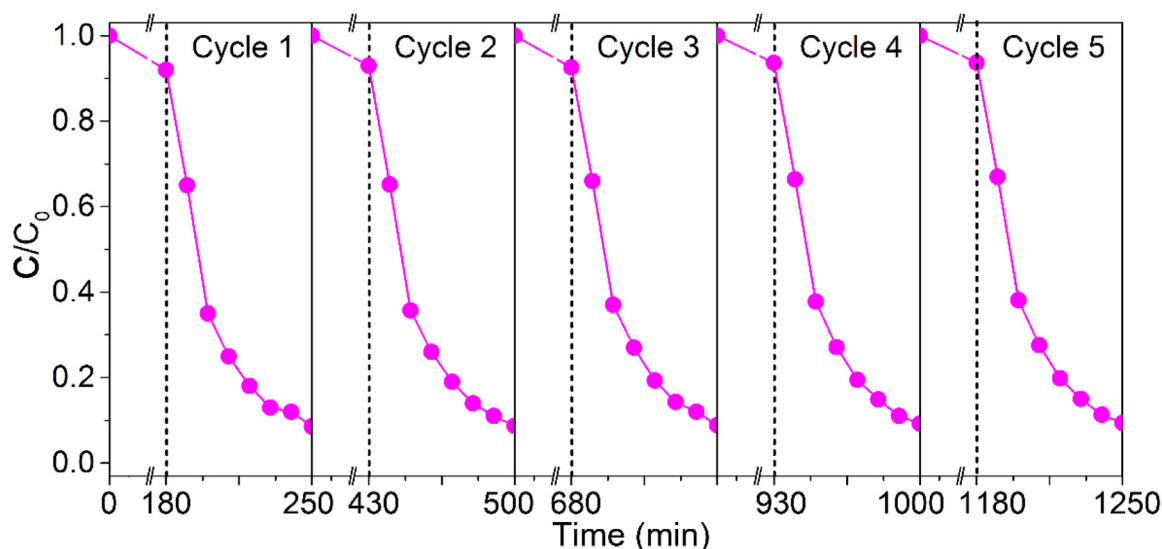
Fig. 7. Total Cr removal by $Mn_3O_4@ZnO/Mn_3O_4$ composite in five cycles under simulated sunlight irradiation.

$Mn_3O_4@ZnO$ photocatalyst and Mn_3O_4 adsorbent were stable and reusable for Cr removal.

3.3. Effects of pH on Cr removal by $Mn_3O_4@ZnO/Mn_3O_4$ composite

As is widely reported, pH plays an important role in photocatalytic reduction of Cr (VI) as well as adsorption process of Cr (III) [40]. The variation of Cr concentration by concurrent photocatalysis and adsorption at different solution pH was displayed in Fig. 8. In the initial adsorption process, $Mn_3O_4@ZnO$ and Mn_3O_4 mixture exhibited superior adsorptive capability in acid condition. Specifically, the mixture achieved 26.0% Cr (VI) adsorption at solution pH = 3.0, more than six times higher than that obtained at solution pH = 12.0. The main species of Cr (VI) at pH = 3.0 was $HCrO_4^-$ (Fig. S7A), and $HCrO_4^-$ could be replaced by CrO_4^{2-} gradually with the rise of solution pH. The isoelectric point of prepared Mn_3O_4 and $Mn_3O_4@ZnO$ were determined to be 4.8 and 9.3 respectively (Fig. S8). Both Mn_3O_4 and $Mn_3O_4@ZnO$ were protonated at pH = 3.0. The positively charged surface of the two nanoparticles could offer advantages for adsorption of negatively charged Cr (VI), resulting in relatively high adsorption efficiency under electrostatic attraction. Accordingly, Mn_3O_4 and $Mn_3O_4@ZnO$ were deprotonated at pH = 12.0 and presented negatively charged surface. Cr (VI) existed in the form of CrO_4^{2-} in the alkaline medium. Then the adsorption efficiency declined due to the electrostatic repulsion between the negatively charged nanoparticles and CrO_4^{2-}.

Moreover, the solution pH dramatically affected the process of Cr (VI) reduction. As shown in Fig. 8B, the photocatalytic reduction of Cr (VI) was enhanced in acid medium. The reduction efficiency reached 97.0% within 30 min at pH = 3.0, much higher than that obtained at pH = 12.0 even within 100 min. Notably, the $Mn_3O_4@ZnO$ photocatalyst achieved 94.0% Cr (VI) reduction within 40 min at pH = 6.0, only a slight decrease compared to that at pH = 3.0. However, the reduction efficiency declined to 42.0% when the solution pH further increased to 12.0.

The species distribution of reductive Cr (III) varied with solution pH, which will affect the Cr (III) adsorption process [41]. Cr (III) mainly existed in the form of Cr^{3+} at pH = 3.0 (Fig. S7B). In this instance, the positively charged Mn_3O_4 adsorbent presented repulsive force to Cr^{3+}, causing low adsorption efficiency and Cr (III) accumulation in the system (Fig. 8C). As a result, the removal rate of total Cr was only 45.0% at pH = 3.0 under simulated sun-

light irradiation for 100 min (Fig. 8A). The Cr^{3+} would combine with OH^- and form $Cr(OH)^{2+}$ and $Cr(OH)_2^+$ with pH rising to 6.0. In this medium, the Mn_3O_4 adsorbent carried negative charges, which could adsorb positively charged $Cr(OH)^{2+}$ and $Cr(OH)_2^+$ effectively. In consequence, the Cr (III) concentration was low during simulated sunlight irradiation. The outstanding performance of total Cr removal (96.0%) was realized within 70 min at pH = 6.0. Also, Cr (III) concentration was low in strongly alkaline medium due to less amount of Cr (III) generated through photocatalysis. In conclusion, Cr (III) adsorption by Mn_3O_4 became the limiting step in total Cr removal at pH lower than 6.0, while Cr (VI) reduction by $Mn_3O_4@ZnO$ dominated at pH higher than 6.0. The optimal pH for Cr removal by $Mn_3O_4@ZnO/Mn_3O_4$ composite was determined as 6.0, at which the synergistic effect of photocatalysis and adsorption was the strongest.

3.4. Mechanism exploration of the enhanced Cr removal efficiency

The optical properties including adsorption boundary and bandgap energy of the Mn_3O_4, $Mn_3O_4@ZnO$ and ZnO were measured by UV–vis diffuse reflectance spectra. As revealed from Fig. 9A, the $Mn_3O_4@ZnO$ photocatalyst was relatively active towards light harvesting in visible light. The adsorption edge of the pure ZnO was observed at around 430 nm. Notably, the $Mn_3O_4@ZnO$ exhibited largely red-shifted adsorption edge (near 700 nm) due to the contribution of Mn_3O_4 component, indicating enhanced photocatalytic activity under visible light irradiation. However, the photo-absorption intensity of $Mn_3O_4@ZnO$ was slightly lower than that of pure Mn_3O_4, which could be attributed to binding effects of pure Mn_3O_4 and ZnO [29]. Moreover, the bandgap energies of pure Mn_3O_4 and ZnO were determined by plotting Kubelka-Munk function $(\alpha h\nu)^2$ versus photon energy ($h\nu$) based on the corresponding absorption edges. The value of bandgap energy was obtained by extending the tangent of the curve and intersecting with $h\nu$ axis. As shown in Fig. 9B, the bandgap energies of Mn_3O_4 and ZnO were estimated to be 2.13 and 3.12 eV respectively, which were in agreement with the values reported in previous studies [30,42].

To better understand the band structure of $Mn_3O_4@ZnO$ composite, the valence band (VB) positions of Mn_3O_4 and ZnO were further detected by XPS-VB spectra. The value of valence band maximum (VBM) can be determined through linear extrapolation method [43]. As shown in Fig. 10, the VBM values of Mn_3O_4 and ZnO
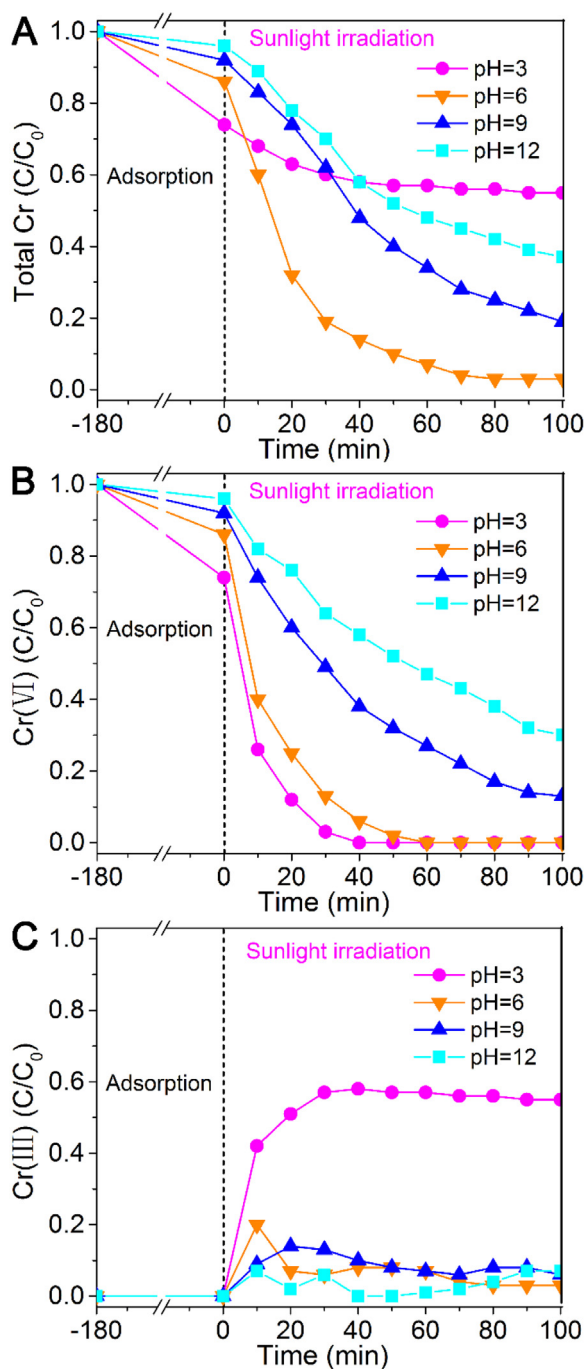
Fig. 8. Effects of solution pH on Cr removal with concurrent photocatalysis and adsorption: (A) total Cr, (B) Cr (VI) and (C) Cr (III). Initial conditions: [Cr (VI)] = C_0 = 10 mg/L, [Mn_3O_4] = 0.15 g/L, Mn_3O_4@ZnO: Mn_3O_4 = 2:1.

were estimated as 1.23 and 2.60 eV respectively. Correspondingly, the conduction band minimum (CBM) values of Mn_3O_4 and ZnO were calculated to be −0.90 and −0.52 eV according to the respective values of band gap energy and VBM. These values determined in this study were similar to the literature ones [44,45].

Fig. 11 schematically illustrated the proposed mechanism of Cr removal with Mn_3O_4@ZnO/Mn_3O_4 composite by concurrent photocatalysis and adsorption under simulated sunlight irradiation. The enhanced photocatalytic activity of Mn_3O_4@ZnO and synergistic effects between Mn_3O_4@ZnO and Mn_3O_4 made great contributions to Cr removal. It was clear that a novel II-type heterojunction was formed when a uniform ZnO layer was precisely

deposited on Mn_3O_4 surface by ALD. The band structures of the two components in Mn_3O_4@ZnO matched very well, which could provide larger driving force for the transfer of photo-generated carriers. In particular, Mn_3O_4 and ZnO would be activated when photo energy was equal to or higher than the bandgap energy, leading to the generation of large amounts of photo-induced electron-hole pairs on Mn_3O_4@ZnO surface. Subsequently, the photo-induced electrons on CB of Mn_3O_4 would migrate immediately to that of ZnO. Meanwhile, the photo-generated holes on VB of ZnO would migrate to that of Mn_3O_4. As a consequence, the electrons and holes were separated and accumulated on different components. This behavior was ascribed to the more negative potentials of VB (1.23 eV) and CB (-0.90 eV) edges for Mn_3O_4 compared to those of corresponding edges (2.60 eV and −0.52 eV) for ZnO. Thus, the efficient separation of photo-generated carriers could be realized. Additionally, the ALD-ZnO layer was uniform, which could also facilitate electron transfer and prevent charge recombination. The electrons collected on CB of ZnO layer could reduce Cr (VI) into Cr (III). Meanwhile, the holes collected on VB of Mn_3O_4 could oxidize H_2O into O_2 [46,47].

In order to better understand the transfer efficiency of photo-excited electrons, the transient photocurrent of Mn_3O_4 and Mn_3O_4@ZnO were measured with several on-off cycles under simulated sunlight irradiation. It can be seen from Fig. 12A that the photocurrents were steady when Mn_3O_4 or Mn_3O_4@ZnO was irradiated by simulated sunlight. The photocurrent sharply reduced to zero as soon as the simulated sunlight was gone. Furthermore, the photocurrents generated by Mn_3O_4 and Mn_3O_4@ZnO exhibited good repeatability during the on-off cycles. Specifically, the Mn_3O_4@ZnO witnessed a higher photocurrent density than pure Mn_3O_4, suggesting the remarkably enhanced efficiency of charge separation [26]. Besides, the electrochemical impedance spectroscopy (EIS) of Mn_3O_4 and Mn_3O_4@ZnO were also recorded to further study the charge transfer efficiency. EIS Nyquist plots of the two samples under simulated sunlight irradiation were depicted in Fig. 12B. As is well known, the diameter of impedance arc directly reflects charge transfer resistance [48]. In comparison with pure Mn_3O_4, Mn_3O_4@ZnO exhibited a smaller diameter of the impedance arc, revealing lower charge transfer resistance. Furthermore, the PL spectra of Mn_3O_4 and Mn_3O_4@ZnO were also collected. As presented in Fig. S9, the pure Mn_3O_4 exhibited a high emission peak at 450 nm. Noticeably, the PL intensity of Mn_3O_4@ZnO decreased significantly, which was almost half compared to that of pure Mn_3O_4. The results indicated the enhanced separation of photo-induced carriers [49,50]. The efficient charge separation and transfer on Mn_3O_4@ZnO composite could enhance the photocatalytic activity, facilitating Cr (VI) reduction.

The XPS spectra of Mn_3O_4@ZnO/Mn_3O_4 after concurrent photocatalysis and adsorption process were recorded to further study the transition behavior of Cr. As shown in Fig. S10A, Mn 2p, Zn 2p and O 1s peaks still appeared in the survey scan. Besides, new peaks of Cr 2p were observed, indicating Cr adsorption onto Mn_3O_4@ZnO/Mn_3O_4 surface. The high resolution Cr 2p spectra in Fig. S10B showed two peaks of Cr 2p1/2 and Cr 2p3/2 locating at 586.3 and 577.1 eV respectively, revealing the adsorbed Cr was in the form of Cr (III) [6]. This phenomenon suggested that Cr (VI) was reduced to Cr (III) by photocatalysis, and the Cr (III) was further removed by adsorption.

Finally, the synergy of photocatalytic reduction and adsorption by Mn_3O_4@ZnO/Mn_3O_4 composite was interpreted. The Mn_3O_4@ZnO was positively charged while Mn_3O_4 was negatively charged in weak acid medium (pH = 6.0). Apparently, most of reduced Cr (III) was immediately adsorbed onto the Mn_3O_4 surface by complexation and ion exchange in the photocatalysis-adsorption system. Thus, more active sites on Mn_3O_4@ZnO surface would be released for photocatalysis, which were employed for
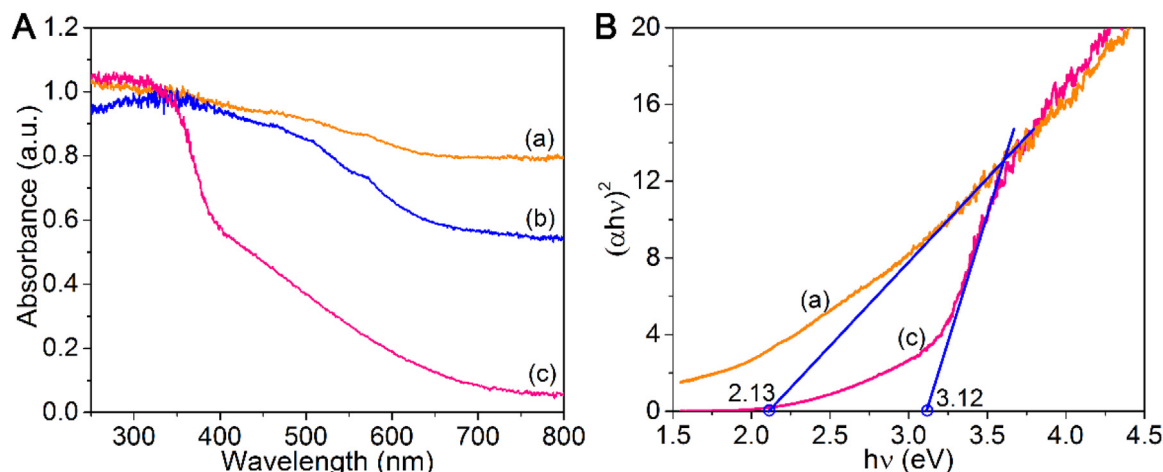
Fig. 9. (A) UV–vis diffuse reflectance spectra; (B) Plots of $(\alpha h\nu)^2$ versus $h\nu$ of the samples: (a) Mn_3O_4; (b) $Mn_3O_4@ZnO$ and (c) ZnO.
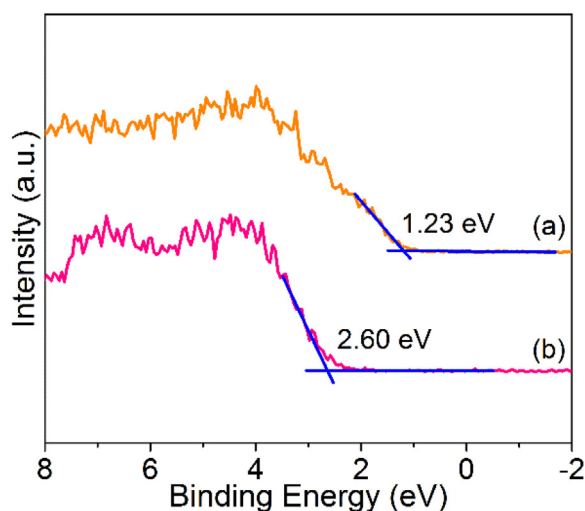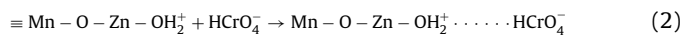

Fig. 10. XPS valance band spectra of (a) Mn_3O_4 and (b) ZnO.

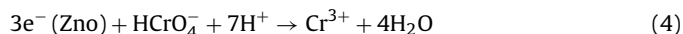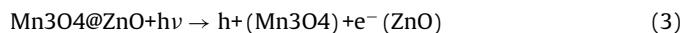continuous Cr (VI) reduction, promoting the photocatalytic efficiency. The synergistic effect between $Mn_3O_4@ZnO$ photocatalyst and Mn_3O_4 adsorbent was favorable for total Cr removal from aqueous solution. For concurrent removal of Cr (VI) and Cr (III)

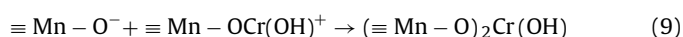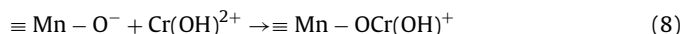at pH = 6.0 under simulated sunlight irradiation, possible reactions were described as follows:

Cr (VI) adsorption by $Mn_3O_4@ZnO$:

$$\equiv Mn - O - Zn - OH + H^+ \rightarrow \equiv Mn - O - Zn - OH_2^+ \qquad (1)$$

$$\equiv Mn - O - Zn - OH_2^+ + HCrO_4^- \rightarrow Mn - O - Zn - OH_2^+ \cdots \cdots HCrO_4^- \qquad (2)$$

Cr (VI) reduction by photocatalysis:

$$Mn3O4@ZnO + h\nu \rightarrow h + (Mn3O4) + e^- (ZnO) \qquad (3)$$

$$3e^- (Zno) + HCrO_4^- + 7H^+ \rightarrow Cr^{3+} + 4H_2O \qquad (4)$$

$$4h + (Mn3O4) + 2H2O \rightarrow O2 + 4H^+ \qquad (5)$$

Cr (III) adsorption by Mn_3O_4:

$$Cr^{3+} + OH^- \rightarrow Cr(OH)^{2+} \qquad (6)$$

$$\equiv Mn - OH \rightarrow \equiv Mn - O^- + H^+ \qquad (7)$$

$$\equiv Mn - O^- + Cr(OH)^{2+} \rightarrow \equiv Mn - OCr(OH)^+ \qquad (8)$$

$$\equiv Mn - O^- + \equiv Mn - OCr(OH)^+ \rightarrow (\equiv Mn - O)_2 Cr(OH) \qquad (9)$$

$$2 \equiv Mn - OH + Cr(OH)^{2+} \rightarrow \equiv (Mn - O)_2 Cr(OH) + 2H^+ \qquad (10)$$

4. Conclusions

In summary, a novel $Mn_3O_4@ZnO/Mn_3O_4$ composite was first employed for Cr (VI) and Cr (III) removal by simulta-
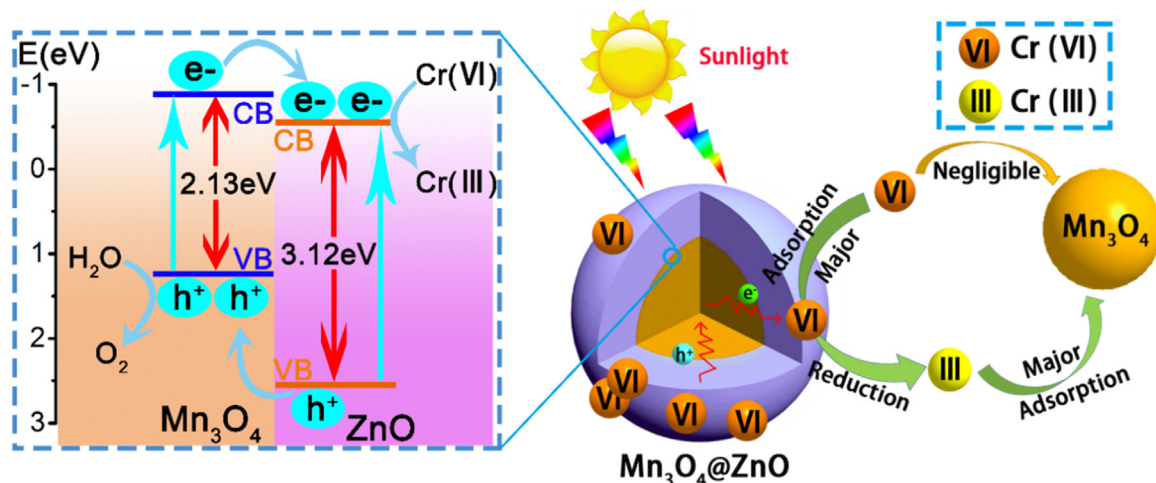

Fig. 11. Schematic illustration of the concurrent photocatalysis and adsorption for Cr removal under simulated sunlight irradiation.
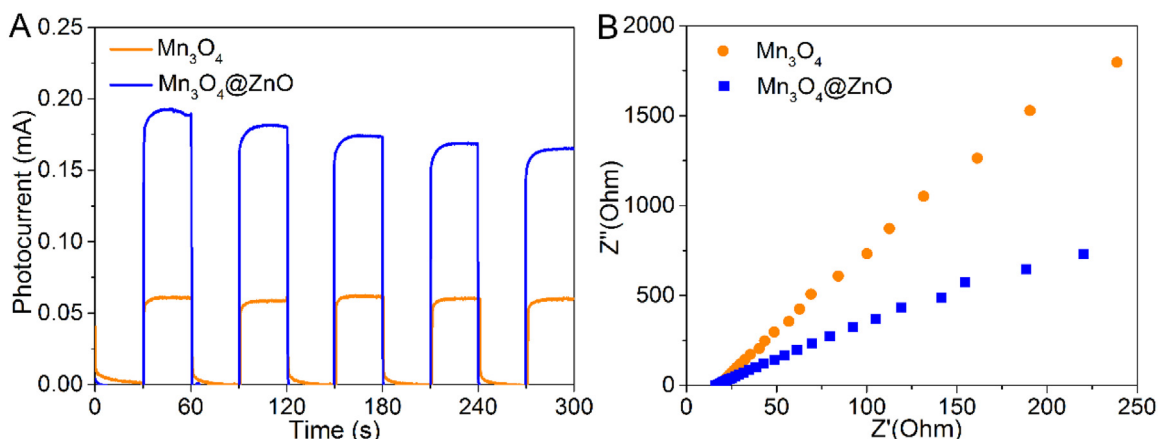
Fig. 12. (A) Photocurrent transient responses with on-off cycles and (B) ESI Nyquist plots of Mn_3O_4 and Mn_3O_4@ZnO under simulated sunlight irradiation.

neous photocatalytic reduction and adsorption, in which the Mn_3O_4@ZnO photocatalyst and Mn_3O_4 adsorbent were synthesized by hydrothermal and ALD method. The highly efficient reduction of Cr (VI) by Mn_3O_4@ZnO was realized under simulated sunlight irradiation because the separation of photo-excited carriers was enhanced by formation of II-type heterojunction and extension of light-response range. Subsequently, the reduced Cr (III) would be desorbed from Mn_3O_4@ZnO surface and immediately transferred onto Mn_3O_4 surface by complexation and ion exchange. This behavior could continuously provide active sites on Mn_3O_4@ZnO surface for photocatalytic reduction of Cr (VI). Thanks to the synergy between Mn_3O_4@ZnO and Mn_3O_4, the Cr (VI) reduction efficiency of 94.0% and total Cr removal rate of 92.0% were achieved within 70 min under simulated sunlight irradiation. Besides, the optimum pH for Cr removal was determined as 6.0 since Cr (III) adsorption and Cr (VI) reduction were the limiting steps for Cr removal at pH < 6.0 and pH > 6.0, respectively. The novel Mn_3O_4@ZnO/Mn_3O_4 composite exhibited excellent performance for Cr (VI) and Cr (III) removal, which would make a significant contribution to remediating Cr contaminated water.

Appendix A. Supplementary data

Supplementary data associated with this article can be found, in the online version, at http://dx.doi.org/10.1016/j.apcatb.2017.05.041.

References

[1] Y. Deng, L. Tang, G. Zeng, Z. Zhu, M. Yan, Y. Zhou, J. Wang, Y. Liu, J. Wang, Appl. Catal. B Environ. 203 (2017) 343–354.
[2] W. Xie, M. Zhang, D. Liu, W. Lei, L. Sun, X. Wang, J. Photochem. Photobiol A 333 (2017) 165–173.
[3] X. Wang, J. Chen, X. Guan, L. Guo, Int. J. Hydrogen Energy 40 (24) (2015) 7546–7552.
[4] K. Zhu, Y. Duan, F. Wang, P. Gao, H. Jia, C. Ma, C. Wang, Chem. Eng. J. 311 (2017) 236–246.
[5] C.C. Wang, X.D. Du, J. Li, X.X. Guo, P. Wang, J. Zhang, Appl. Catal. B Environ. 193 (2016) 198–216.
[6] W. Liu, J. Ni, X. Yin, Water Res. 53 (2014) 12–25.
[7] J.P. Squifflet, Y.D. Pirson, A.N. Dardenne, P.J. Van Cangh, Y.d.S.C. Van, G.P. Alexandre, Chem. Eng. J. 262 (2015) 1144–1151.
[8] F. Liu, J. Yu, G. Tu, L. Qu, J. Xiao, Y. Liu, L. Wang, J. Lei, J. Zhang, Appl. Catal. B Environ. 201 (2017) 1–11.
[9] J. Gorny, G. Billon, C. Noiriel, D. Dumoulin, L. Lesven, B. Madé, Environ. Rev. 24 (2016) 503–516.
[10] B. Xie, C. Shan, Z. Xu, X. Li, X. Zhang, J. Chen, B. Pan, Chem. Eng. J. 308 (2016) 791–797.
[11] F.M.M. Paschoal, M.A. Anderson, M.V.B. Zanoni, J. Hazard. Mater. 166 (2009) 531–537.
[12] Y. Bai, L. Ye, T. Chen, P. Wang, L. Wang, X. Shi, P.K. Wong, Appl. Catal. B Environ. 203 (2017) 633–640.
[13] Q. Cheng, C. Wang, K. Doudrick, C.K. Chan, Appl. Catal. B Environ. 176–177 (2015) 740–748.
[14] C. Mondal, M. Ganguly, J. Pal, A. Roy, J. Jana, T. Pal, Langmuir 30 (2014) 4157–4164.
[15] G. Chen, J. Feng, W. Wang, Y. Yin, H. Liu, Water Res. 108 (2016) 383–390.
[16] M.D.L. Cruz, D.S. Martínez, E.L. Cuéllar, Solid State Sci. 12 (2010) 88–94.
[17] J.C. Wang, J. Ren, H.C. Yao, L. Zhang, J.S. Wang, S.Q. Zang, L.F. Han, Z.J. Li, J. Hazard. Mater. 311 (2016) 11–19.
[18] H. Xu, J. Yan, X. She, L. Xu, J. Xia, Y. Xu, Y. Song, L. Huang, H. Li, Nanoscale 6 (2014) 1406–1415.
[19] J. Su, Y. Zhang, S. Xu, S. Wang, H. Ding, S. Pan, G. Wang, G. Li, H. Zhao, Nanoscale 6 (2014) 5181–5192.
[20] X.F. Lei, X.X. Xue, H. Yang, Appl. Surf. Sci. 321 (2014) 396–403.
[21] Q. Wu, J. Zhao, G. Qin, C. Wang, X. Tong, X. Song, Appl. Catal. B Environ. 142–143 (2013) 142–148.
[22] S. Rengaraj, S. Venkataraj, J.W. Yeon, Y. Kim, X.Z. Li, G.K.H. Pang, Appl. Catal. B Environ. 77 (2007) 157–165.
[23] D.R. Lindsay, K.J. Farley, R.F. Carbonaro, J. Environ. Monit. 14 (2012) 1789–1797.
[24] J. Chen, P. Yang, D. Song, S. Yang, L. Zhou, L. Han, B. Lai, Front. Environ. Sci. Eng. Chin. 8 (2014) 960–966.
[25] F. Duan, C. Chen, X. Zhao, Y. Yang, X. Liu, Y. Qin, Environ. Sci. Nano 3 (2016) 213–222.
[26] J. Zhao, J. Nan, Z. Zhao, N. Li, J. Liu, F. Cui, Appl. Catal. B Environ. 202 (2017) 509–517.
[27] S.A. Asif, S.B. Khan, A.M. Asiri, Nanoscale Res. Lett. 1 (2015) 355.
[28] Y. Xu, H. Xu, H. Li, J. Xia, C. Liu, L. Liu, J. Alloys Compd. 509 (2011) 3286–3292.
[29] N. Li, J. Zhang, Y. Tian, J. Zhao, J. Zhang, W. Zuo, Chem. Eng. J. 308 (2017) 377–385.
[30] M.T. Qamar, M. Aslam, Z.A. Rehan, M.T. Soomro, J.M. Basahi, I.M.I. Ismail, T. Almeelbi, A. Hameed, Appl. Catal. B Environ. 201 (2016) 105–118.
[31] D. Lu, W. Chai, M. Yang, P. Fang, W. Wu, B. Zhao, R. Xiong, H. Wang, Appl. Catal. B Environ. 190 (2016) 44–65.
[32] N. Li, J. Zhang, Y. Tian, J. Zhao, J. Zhang, W. Zuo, Chem. Eng. J. 304 (2016) 165–174.
[33] Y. Cantu, A. Remes, A. Reyna, D. Martinez, J. Villarreal, H. Ramos, S. Trevino, C. Tamez, A. Martinez, T. Eubanks, Chem. Eng. J. 254 (2014) 374.
[34] Z.Y. Tian, P.M. Kouotou, N. Bahlawane, P.H.T. Ngamou, J. Phys. Chem. C 117 (2013) 6218–6224.
[35] G. Wang, X. Peng, L. Yu, G. Wan, S. Lin, Y. Qin, J. Mater. Chem. A 3 (2015) 2734–2740.
[36] M. Karimi, M.J. Eshraghi, J. Alloys Compd. 696 (2017) 171–176.
[37] Q. Luo, X. Yang, X. Zhao, D. Wang, R. Yin, X. Li, J. An, Appl. Catal. B Environ. 204 (2017) 304–315.
[38] K.S.W. Sing, R.T. Williams, Adsorpt. Sci. Technol. 22 (2004) 773–782.
[39] R. Yuan, S.N. Ramjaun, Z. Wang, J. Liu, Chem. Eng. J. 192 (2012) 171–178.
[40] B.A. Marinho, R.O. Cristóvão, R. Djellabi, J.M. Loureiro, A.R.B. Rui, V.J.P. Vilar, Appl. Catal. B Environ. 203 (2017) 18–30.
[41] M. Kebir, M. Trari, R. Maachi, N. Nasrallah, B. Bellal, A. Amrane, J. Environ. Chem. Eng. 3 (2015) 548–559.

[42] P.N. Paulino, V.M.M. Salim, N.S. Resende, Appl. Catal. B Environ. 185 (2015) 362–370.

[43] Y.P. Xie, Z.B. Yu, G. Liu, X.L. Ma, H.M. Cheng, Energy Environ. Sci. 7 (2014) 1895–1901.

[44] S. Bag, K. Roy, C.S. Gopinath, C.R. Raj, ACS Appl. Mater. Interfaces 6 (2014) 2692–2699.

[45] Y. Lv, C. Pan, X. Ma, R. Zong, X. Bai, Y. Zhu, Appl. Catal. B Environ. 138-139 (2013) 26–32.

[46] S. Nayaka, L. Mohapatra, K. Parida, J. Mater. Chem. A 3 (2015) 18622–18635.

[47] Y. Li, W. Cui, L. Liu, R. Zong, W. Yao, Y. Liang, Y. Zhu, Appl. Catal. B Environ. 199 (2016) 412–423.

[48] Y. Yang, X.J. Li, J.T. Chen, L.Y. Wang, J. Photochem. Photobiol. A 163 (2004) 517–522.

[49] J. Li, M. Zhang, Z. Guan, Q. Li, C. He, J. Yang, Appl. Catal. B Environ. 206 (2017) 300–307.

[50] S. Stojadinović, N. Radić, R. Vasilić, M. Petković, P. Stefanov, L. Zeković, B. Grbić, Appl. Catal. B Environ. 126 (2012) 334–341.